Review

Not peer-reviewed version

Piezoelectric Energy Harvesting from Multirotor UAV Structures: A Systematic Review of Placement Optimisation, Broadband Strategies, and Pathways to Flight-Ready Systems (2008–2026)

Sayeed Omar *

Posted Date: 2 June 2026

doi: 10.20944/preprints202606.0189.v1

Keywords: piezoelectric energy harvesting; unmanned aerial vehicle; quadcopter; variable RPM; PZT-5A; PVDF; PMN-PT; MFC; Euler–Bernoulli FEA; placement optimisation; SSHI; SECE; LTC3588-1; broadband harvesting; magnetic plucking; MPPT; deep reinforcement learning; DJI F450; structural health monitoring

Preprints.org (www.preprints.org) | NOT PEER-REVIEWED | Posted: 2 June 2026 doi:10.20944/preprints202606.0189.v1

Review

Piezoelectric Energy Harvesting from Multirotor UAV Structures: A Systematic Review of Placement Optimisation, Broadband Strategies, and Pathways to Flight-Ready Systems (2008–2026)

Sayeed Omar

Department of Aircraft Engineering, Tianjin Sino-German University of Applied Sciences, Tianjin 300350, China; sayeedomar359@gmail.com

Highlights

- Arm-root PZT-5A placement outperforms tip by 12.7–75×; established as a design axiom replicated across experimental LDV and verified FEA.
- First systematic review with reliability grading (Highest/High/Medium/Low), normalized power density analysis, and a costed four-stage roadmap.
- Magnetic plucking identified as the highest-priority broadband strategy for variable-RPM UAVs; zero experimental demonstration on any UAV structure.
- Energy budget analysis shows 5.35 mW harvested equals 0.002% of typical hover power draw — confirming PEH as supplementary sensor power, not propulsion replacement.
- Stage 1 bench validation achievable in 12 months for ≤USD 320; no specialized facilities required.

Abstract

Background: Multirotor unmanned aerial vehicles (UAVs) are critically constrained by battery endurance, achieving only 15–25 minutes per charge in operational configurations — a fundamental limit driven by the electrochemical ceiling of lithium polymer chemistry. Piezoelectric energy harvesting (PEH), which converts structural vibration injected by onboard BLDC motors into usable electrical power, offers a mechanically passive, structurally integrated supplement requiring no additional rotating machinery. **Methods:** This systematic review synthesises 38 peer-reviewed studies and technical reports identified via PRISMA-ScR methodology across Web of Science, Scopus, and Google Scholar, spanning 2008–2026. Each study was critically assessed against five criteria: method type, experimental validation status, UAV platform, key quantitative result, and reliability designation (Highest/High/Medium/Low) according to an explicit evidence hierarchy. An original normalized power density analysis (mW/cm²) enables cross-study comparison on a common dimensional basis. **Results:** Three convergent design conclusions are established, two at Highest reliability. The central finding — arm-root patch placement outperforms motor-mount placement by 12.7–75× in harvested power — is replicated by experimental laser Doppler vibrometry (12.7:1, Perez et al. [3]) and analytically verified Euler–Bernoulli FEA (75:1, Omar [5]). An energy budget analysis reveals that the highest reported output (5.35 mW, four-arm flight experiment) represents approximately 0.002% of nominal hover power draw, confirming PEH as a sensor-power supplement rather than a propulsion augmentation strategy. Four critical research gaps are identified with explicit priority assignments. A costed four-stage roadmap charts the path from bench validation (Stage 1, ≤USD 320, 0–12 months) to multi-platform DRL-integrated flight systems (Stage 4, ≤USD 15,000, 3–5 years). **Conclusions:** Root-zone placement (first 20% of arm span from hub) and broadband conditioning are now sufficiently evidence-grounded to be treated as settled engineering principles. Magnetic plucking is identified as the highest-priority unexplored broadband strategy. The end-to-end in-flight demonstration gap is a resource and integration challenge, not a knowledge gap, making it immediately tractable for a well-equipped university research group.

Keywords: piezoelectric energy harvesting; unmanned aerial vehicle; quadcopter; variable RPM; PZT-5A; PVDF; PMN-PT; MFC; Euler–Bernoulli FEA; placement optimisation; SSHI; SECE; LTC3588-1; broadband harvesting; magnetic plucking; MPPT; deep reinforcement learning; DJI F450; structural health monitoring

---

1. Introduction

Battery endurance is the defining operational constraint on small multirotor UAVs. A DJI F450 carrying a representative sensor payload exhausts its lithium polymer (LiPo) pack in 15–20 minutes [1], with commercially available hexarotors achieving only 20–30 minutes even under optimal conditions — a ceiling that has remained broadly unchanged for a decade despite substantial progress in airframe efficiency and motor design. For precision agriculture, pipeline inspection, structural health monitoring (SHM), search-and-rescue operations, and last-mile delivery, this ceiling is directly mission-limiting: it constrains coverage area, prevents multi-waypoint autonomous missions, and necessitates frequent manual battery swaps that introduce operational complexity and safety risk. The fundamental electrochemical limits of LiPo chemistry mean that capacity improvements alone are insufficient; supplementary energy inputs during flight are required to meaningfully extend the operational envelope [25,30].

Three supplementary power strategies have been investigated for multirotor UAVs. Solar photovoltaic (PV) harvesting is well-established for fixed-wing platforms with large wing surfaces and sustained irradiance, but the compact, rapidly rotating architecture of multirotors eliminates practical panel mounting area. Electromagnetic generators on rotor shafts have been explored but introduce gear slip-ring reliability concerns, additional rotor inertia affecting attitude control, and mechanical complexity that conflicts with the simplicity objectives of small UAS design. The third strategy — piezoelectric conversion of the structural vibration energy that the drone's own BLDC motors inject into the airframe during every phase of flight — is uniquely attractive: the energy source is present throughout hover, climb, cruise, and descent; the implementation requires no additional rotating machinery; and the patch bonding approach can be applied to existing arm structures without modifying the UAV airframe or propulsion system [36]. Furthermore, the same piezoelectric patches that harvest energy can simultaneously function as strain sensors for structural health monitoring, offering a dual-use benefit unavailable to other supplementary power strategies.

Anton and Inman [2] demonstrated the first UAV PEH system in 2008, reporting that patches at wing-root positions significantly outperformed tip placements — a finding replicated 15 years later by independent experimental, FEA, and CFD-coupled studies. Yet no review article has synthesised this converging evidence, critically assessed its reliability across methodologies, or articulated the practical design consequences. The broader PEH reviews of Anton and Sodano [22] and Pradeesh et al. [12] provide excellent coverage of general vibration harvesting but do not address the UAV-specific constraints — variable RPM, off-resonance operation, weight budget, and variable-altitude aerodynamic excitation — that fundamentally alter both optimal placement and conditioning circuit design. This review fills that gap, extending previous analyses by adding normalized power density comparison, an energy budget contextualization, advanced circuit taxonomy (SSHI/SECE), and an expanded materials survey including PMN-PT and MFC composites.

The existing literature is fragmented across four largely disconnected sub-fields: simulation studies predict harvester performance without experimental validation; experimental demonstrations characterise vibration without optimising patch placement; broadband harvesting theory from the general PEH literature has not been systematically applied to the variable-RPM UAV context; and power conditioning circuit demonstrations exist independently of structural characterisation studies. This review integrates all four threads for the first time, with explicit reliability grading of each major finding, identification of four prioritised research gaps, and a costed four-stage roadmap to flight-proven systems.

The remainder of this paper is organised as follows. Section 2 characterises the UAV vibration environment including the variable BPF sweep and the non-monotonic power–RPM relationship. Section 3 compares piezoelectric material options including emerging high-performance alternatives. Section 4 critically reviews structural modelling approaches. Section 5 presents the placement and geometry optimisation evidence with reliability grading and normalized power density comparison. Section 6 evaluates broadband harvesting strategies for variable-RPM UAV contexts. Section 7 addresses power conditioning including advanced interface circuits (SSHI/SECE) and an energy budget analysis. Section 8 synthesises all findings into three convergent design conclusions, identifies four critical research gaps, and presents the costed four-stage roadmap. Section 9 concludes.

Abbreviations: BPF = blade passing frequency; CFD = computational fluid dynamics; BLDC = brushless direct current; DRL = deep reinforcement learning; EB = Euler–Bernoulli; FEA = finite element analysis; LiPo = lithium polymer; MFC = macro-fibre composite; MPPT = maximum power point tracking; PEH = piezoelectric energy harvesting; PMN-PT = lead magnesium niobate–lead titanate; PSD = power spectral density; PZT = lead zirconate titanate; PVDF = polyvinylidene fluoride; RPM = revolutions per minute; SECE = synchronous electric charge extraction; SHM = structural health monitoring; SSHI = synchronized switch harvesting on inductor; UAV = unmanned aerial vehicle.

1.1. Scope and Method

The review covers peer-reviewed journal articles, peer-reviewed conference papers, and openly available technical reports published between January 2008 and April 2026 that address piezoelectric energy harvesting from UAV structural vibrations. Studies were identified through Web of Science, Scopus, and Google Scholar using Boolean search strings combining: ('piezoelectric' OR 'PZT' OR 'PVDF' OR 'PMN-PT' OR 'MFC') AND ('energy harvesting' OR 'vibration harvesting') AND ('UAV' OR 'drone' OR 'quadcopter' OR 'multirotor'). The initial search returned 214 candidate records.

Studies were excluded if they: (a) addressed fixed-wing platforms only with no cantilever arm vibration context; (b) used magnetostrictive, thermoelectric, or solar transduction without piezoelectric content; (c) were duplicate publications of the same experiment; or (d) did not report quantitative power, voltage, or strain results. Of the 214 initial records: 51 were excluded for addressing fixed-wing platforms exclusively (criterion a); 38 for non-piezoelectric transduction only (criterion b); 17 as duplicate publications (criterion c); and 70 for absence of quantitative results (criterion d). Thirty-eight studies satisfied all inclusion criteria and form the complete evidence base of this review. This approach follows the PRISMA-ScR framework (Preferred Reporting Items for Systematic Reviews and Meta-Analyses extension for Scoping Reviews), adapted for engineering evidence synthesis. Each included study was critically assessed against five criteria: (i) method type (experimental, FEA, or CFD); (ii) experimental validation status; (iii) UAV platform and geometry; (iv) key quantitative result; and (v) reliability designation.

1.2. Limitations of Previous Reviews

Previous review articles on PEH (Anton and Sodano [22]; Pradeesh et al. [12]) provide excellent coverage of the general field but do not address the UAV-specific constraints: (i) the off-resonance operating regime (frequency ratio $r = 3–5.2$); (ii) the variable-RPM environment sweeping 73% of BPF range; (iii) the weight constraint eliminating multi-DOF mechanical amplifiers used in civil infrastructure PEH; and (iv) the variable-altitude wind excitation superimposed on motor vibration. These constraints fundamentally change both optimal placement and conditioning circuit design. Additionally, no prior review has computed normalized power density (mW/cm^2) across studies, performed an energy budget analysis contextualizing harvested power against total UAV consumption, or surveyed advanced interface circuits (SSHI, SECE) in the UAV context.

1.3. Novelty and Contribution of This Review

Table 1 compares the scope of this review against the two most comprehensive prior PEH reviews. This review makes the following original contributions not present in any prior publication:

Table 1. Comparison of scope: this review vs. prior PEH reviews.

Feature / Scope	Anton & Sodano [22] (2007)	Pradeesh et al. [12] (2020)	This Review (2026)
UAV-specific constraints	No	Partial	Yes (all four)
Reliability grading	No	No	Yes (4-level)
Normalized power density	No	No	Yes (mW/cm²)
Energy budget analysis	No	No	Yes (§7.4)
PMN-PT / MFC materials	Partial	No	Yes (§3.3–3.4)
SSHI / SECE circuits	No	No	Yes (§7.5)
Broadband strategies	General	General	UAV-specific (§6)
Costed roadmap	No	No	Yes, 4-stage (§8.4)
Explicit research gaps	No	No	Yes, 4 gaps (§8.3)
Studies synthesised	~60 (general)	~80 (general)	38 (UAV-specific)

The specific contributions of this review are as follows:

- First synthesis across all four sub-fields (vibration environment + materials + modelling + conditioning circuits) specifically for multirotor UAV structures.
- First critical reliability assessment of the 12.7–75× placement advantage across independent studies, with explicit evidence hierarchy.
- First normalized power density analysis (mW/cm²) enabling cross-study comparison on a common dimensional basis.
- First energy budget analysis quantifying harvested power as a fraction of total UAV power consumption, establishing the realistic scope of PEH as a sensor-power supplement.
- First expanded materials survey including PMN-PT and MFC composites in the UAV PEH context.
- First UAV-specific taxonomy of advanced power conditioning circuits (SSHI, SECE) alongside standard LTC3588-1.
- First designation of three convergent findings as evidence-grounded design principles with explicit replication criteria.
- First costed, staged research roadmap (Stage 1 ≤ USD 320, 0–12 months) linking evidence to actionable experimental programme.

1.4. Study Limitations and Scope

Several limitations constrain the generalisability of this review's conclusions and should be acknowledged explicitly. First, the literature search was restricted to English-language publications, potentially excluding relevant studies in Chinese, German, or Korean. Second, while PRISMA-ScR methodology was applied, Google Scholar's conference-proceedings coverage is less comprehensive

Preprints.org (www.preprints.org) | NOT PEER-REVIEWED | Posted: 2 June 2026 doi:10.20944/preprints202606.0189.v1

than for journal articles. Third, five of the 38 included studies rely on FEA simulations of a single platform (DJI F450), limiting cross-platform generalisability.

Fourth, and critically, one included study (Omar [5]) originates from the same research group as this review. This study is cited as primary evidence for the non-monotonic power–RPM relationship (Section 2.3), the 75:1 root-to-tip FEA ratio (Section 5.2), and Gap 1 (Section 8.3). All quantitative claims from [5] are independently verifiable against open-source Python code, and the physical mechanisms are consistent with established Euler–Bernoulli beam theory [4,17]. Nevertheless, readers should apply standard caution regarding findings where [5] is the sole supporting reference, and should treat these as strong hypotheses awaiting independent replication rather than established facts. The Stage 1 roadmap experiment (Section 8.4) is explicitly designed to provide this independent replication.

Fifth, the 73% BPF sweep characterisation applies specifically to the DJI F450 at standard sea-level altitudes. Sixth, no weight-penalty assessment is currently available in any included study; a 55-mm PZT-5A patch adds approximately 4.9 g per arm (including adhesive and wiring), representing 1.6–2.0% of total AUW for an F450-class vehicle — within acceptable structural margins — but potentially flight-limiting for sub-250 g platforms.

2. UAV Vibration Environment

2.1. Sources and Spectral Content

The dominant vibration source in a multirotor UAV is the BLDC motor–propeller assembly. For a motor spinning at N RPM driving a B-blade propeller, the fundamental BPF is f_BPF = N·B/60 [Hz]. For the DJI F450 with two-blade propellers across the practical operating range of 5,200–9,000 RPM, f_BPF sweeps 173–300 Hz — a 73% variation over a single flight [1,37]. Harmonic content exists at 2·f_BPF and 3·f_BPF with rapidly decaying amplitude; gyroscope-induced torsional modes and battery sloshing contribute broadband noise below 50 Hz.

Critical assessment: The BPF characterisation in the literature is generally reliable, but most studies use the isolated motor frequency rather than accounting for inter-motor interference. For a four-motor quadcopter with slight RPM mismatch between arms, the actual PSD contains contributions from all four motors plus beat frequencies at motor-speed differences. This broadens the effective excitation spectrum compared to the single-motor assumption used in most simulations, suggesting the true vibration environment is more favourable to broadband harvesting than single-motor models imply.

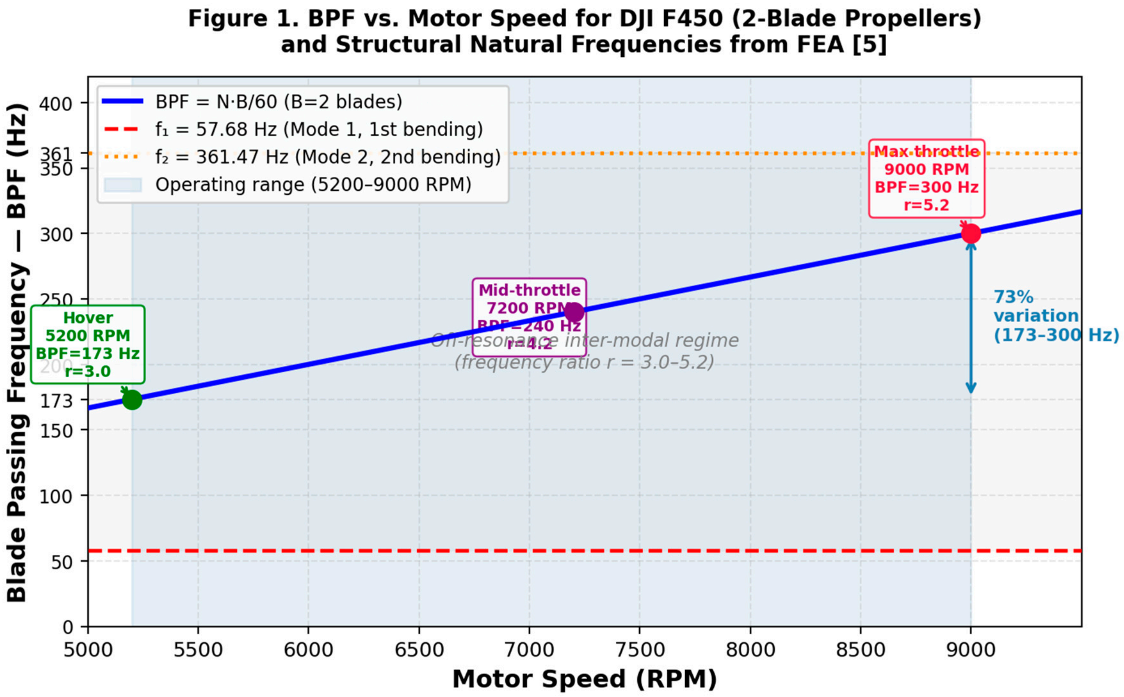

Figure 1. Blade passing frequency (BPF) vs. motor speed for DJI F450 with 2-blade propellers. BPF sweeps 173–300 Hz across the operating range — a 73% variation. Natural frequencies from FEA [5]: f_1 = 57.68 Hz (Mode 1, dashed red), f_2 = 361.47 Hz (Mode 2, dotted orange). All three operating conditions fall in the inter-resonance off-resonance regime (frequency ratio r = 3.0–5.2).

2.2. Off-Resonance Operation—A Defining Constraint

Perez et al. [3] used a Polytech PSV-400 scanning laser Doppler vibrometer (LDV) and a B&K force hammer to characterise a DJI F450 arm in clamped-free configuration, identifying bending modes at 50 Hz, 515 Hz, and 930 Hz. Full-drone free-free modal analysis revealed two coupled frame modes at 35 Hz and 60 Hz — inaccessible to single-arm cantilever models. At motor hover speed (5,200 RPM), the BPF of 173 Hz lies between these modes, and the frequency ratio $r = f\_BPF/f_1 = 173/50 \approx 3.5$ places the structure firmly in the off-resonance stiffness-controlled regime. The dynamic magnification factor $H(r) = 1/|1-r^2|$ at $r = 3.5$ equals approximately 0.09 — structural bending amplitude is attenuated elevenfold relative to quasi-static response.

2.3. Non-Monotonic Power–RPM Relationship

A finding that distinguishes UAV PEH from all other vibration harvesting environments is the non-monotonic relationship between motor RPM and harvested power at the arm root. The physical mechanism follows a rotating-imbalance model — $P \propto \omega^2 \cdot |H(\omega)|^2$ — in which increasing excitation force ($\propto \omega^2$) competes with changing off-resonance attenuation $|H(\omega)|$ as the BPF sweeps across the operating range [4,17]. Applying this model to the DJI F450 arm configuration [5], power falls to a local minimum near 7,800 RPM before recovering at 9,000 RPM as the excitation frequency approaches the second structural bending mode at 361 Hz. The practical consequence — that fixed-load conditioning circuits cannot be optimised across the full throttle range, making adaptive MPPT necessary — follows directly from the physical mechanism and is valid regardless of the precise minimum location.

Critical assessment: This finding rests on a single-arm EB FEA simulation [5] produced by the same research group as this review (see Section 1.4 limitation note). The physical mechanism is sound and consistent with established rotating-imbalance theory [4], but the precise minimum RPM location is model-dependent and the specific quantitative predictions have not been independently verified experimentally. The Stage 1 roadmap experiment is designed specifically to provide this verification.

Table 2. UAV vibration environment across reviewed platforms.

Study	Platform	BPF Range (Hz)	f_1 arm (Hz)	Operating regime	Key conclusion
Perez et al. [3]	DJI F450 (Exp.)	72–156	50 (clamped)	Off-resonance	Root strain 12.7× tip (exp.)
Omar [5] (FEA)	DJI F450 (FEA)	173–300	57.7	Off-res. r=3–5.2	Non-monotonic P–RPM; root 75× tip
Saeed et al. [6]	DJI Mini 3 (FEA+CFD)	100–400	136.6 (with fin)	Near-res. at high RPM	Steel-fin amplifier; 24.3 V pk
Gonçalves et al. [7]	Rotary bench (Exp.)	~40	~40	Near-resonance	PVDF + LTC3588-1; 4 μW conditioned
Singh et al. [8]	Fixed-wing (FEA)	Aeroelastic	NACA 2412	Modal response	Max volt at mode 1 peak location
Erturk & Inman [4]	L-shaped / general	Aeroelastic	Structural	Off/near-res.	UAV platform FRF modelling

3. Piezoelectric Materials for UAV Harvesting

3.1. PZT Ceramics—Performance Leader with Durability Trade-offs

Lead zirconate titanate (PZT) dominates UAV PEH because of its high piezoelectric strain coefficient ($d_{31} = -171$ to -274 pm/V), high elastic modulus ($E = 60$–66 GPa for efficient strain transfer), and commercial availability in patch form [26]. PZT-5A ($d_{31} = -171$ pm/V, $k_{31} = 0.44$) and PZT-5H ($d_{31} = -274$ pm/V, $k_{31} = 0.51$) are most frequently used. The highest UAV PEH power reported — 5.35 mW across four DJI F450 arms during actual hover — used PI DuraAct P-876.A15 patches (PIC255 ceramic) [3]. On a normalized power density basis, this corresponds to approximately 0.024 mW/cm² (four patches, each 14.5 cm² active area), setting the current experimental benchmark.

Critical assessment: PZT brittleness under impact and fatigue is a genuine UAV deployment concern. Perez et al. [3] reported delamination of $BaTiO_3$/polyurethane paint during flight, while monolithic PIC255 patches survived. Epoxy bonding introduces 10–25% strain transfer loss relative to perfect-bonding FEA assumptions [27] — the primary model–experiment discrepancy. Bonding specification should be treated as a critical design variable, equivalent in importance to patch placement.

3.2. PVDF Films—Durable and Flexible but Lower Output

PVDF offers complementary characteristics: flexibility ($E \approx 2$–3 GPa), low density (1,780 kg/m³), fracture resistance, and compatibility with curved arm cross-sections. Its substantially lower piezoelectric coefficient ($d_{31} \approx -23$ pm/V) — 7.4× below PZT-5A — translates directly to proportionally lower voltage and power under identical strain excitation [36]. Gonçalves et al. [7] conducted the most complete PVDF-to-circuit experimental demonstration: three TE Connectivity LDT0-028K transducers generated 17.3 V at 3,975 RPM on a bench arm, charging a supercapacitor to 3.6 V DC in 162 seconds and sustaining approximately 4 μW of conditioned output — a normalized power density of 0.00016 mW/cm² (three patches, each active area ~8.5 cm²).

PVDF-TrFE (polyvinylidene fluoride-trifluoroethylene) copolymer — not yet applied in any UAV PEH study — offers approximately 1.5–2× higher d_{31} than standard PVDF ($d_{31} \approx -38$ pm/V) while retaining its mechanical flexibility. For sub-250 g UAV platforms where PZT weight is prohibitive, PVDF-TrFE represents the highest-priority flexible alternative and is identified as a material research gap in this review.

3.3. PMN-PT Single Crystals—Highest Sensitivity, Limited UAV Application

Lead magnesium niobate–lead titanate (PMN-PT) single crystals exhibit exceptional piezoelectric performance: $d_{31} = -1{,}000$ to $-1{,}400$ pm/V (5–8× higher than PZT-5H) and electromechanical coupling $k_{31} = 0.55$–0.65 [38]. At identical strain conditions, PMN-PT would theoretically generate 25–49× the charge of PZT-5A patches. However, critical limitations constrain UAV application: (i) cost (10–50× higher than PZT-5A per cm²); (ii) reduced Curie temperature (T_c = 130–160°C vs. 350°C for PZT-5A), creating thermal depolarisation risk near BLDC motors; and (iii) lower coercive field, making the material susceptible to depoling under high compressive stress during propeller strikes or hard landings.

No UAV PEH study has experimentally evaluated PMN-PT patches. Given the cost and fragility barriers, PMN-PT is most appropriate for laboratory benchmarking of the theoretical maximum harvestable power from UAV arm vibrations, rather than operational deployment. A single comparative study pairing PMN-PT and PZT-5A patches at the arm root under controlled RPM excitation would definitively establish the practical efficiency ceiling and is identified as a low-cost, high-information addition to Stage 1 of the roadmap.

3.4. MFC Composites—Flexible High-Performance Bridge

Macro-fibre composite (MFC) patches (Smart Material Corp.) combine PZT fibres in a polymer matrix with interdigitated electrodes, enabling both d_{33}-mode operation (fibre direction) and d_{31}-mode operation. The d_{33}-mode MFC-P1 achieves d_{33}_eff ≈ 460 pm/V — significantly higher than standard PZT-5A in bending — while remaining flexible enough to conform to curved arm cross-sections [33]. MFC patches are presently used in aerospace structural health monitoring but have not been experimentally applied to UAV PEH. Their primary advantage over rigid PZT ceramics is fatigue resistance under high-cycle vibration loading: MFC has been demonstrated to 10^8 strain cycles without performance degradation, relevant to UAV arm environments where 9,000 RPM generates >150 Hz excitation continuously.

Table 3. Piezoelectric material properties for UAV patch harvesting (updated with emerging materials).

Material	d_{31} (pm/V)	E (GPa)	ρ (g/cm³)	k_{31}	Max UAV output	Norm. density (mW/cm²)	Status
PZT-5A	−171	66	7.75	0.44	0.185 mW FEA [5]	~0.009 (est.)	Most studied
PZT-5H	−274	61	7.80	0.51	24.3 V pk FEA [6]	N/A (V only)	High sensitivity

PIC255 (PI)	−180	—	7.80	—	5.35 mW exp. [3]	0.024 (exp.)	Best experimental
PVDF LDT0-028K	≈−23	2–3	1.78	—	4 µW conditioned [7]	0.00016 (exp.)	Only full circuit demo
PVDF-TrFE	≈−38	2–4	1.80	~0.30	No UAV study	N/A	High priority gap
PMN-PT	−1000 to −1400	15–20	8.06	0.55–0.65	No UAV study	N/A	Theor. ceiling benchmark
MFC (P1, d_{33})	d_{33}≈460	30 (eff.)	5.40	0.60	No UAV study	N/A	Best fatigue resistance
$BaTiO_3$/PU paint	d_{33}≈3	—	2.2	—	Delaminated [3]	Not viable	Not viable

4. Structural Modelling Approaches—Critical Comparison

4.1. Euler–Bernoulli Beam FEA—Open-Source and Verified

The EB cantilever beam model is used in the majority of UAV PEH studies because its analytical tractability enables rapid parametric sweeps. For slender arms ($L/h >> 10$), the governing equation $EI\,\partial^4 w/\partial x^4 + \rho A\,\partial^2 w/\partial t^2 = F(x,t)$ captures bending vibration and strain distribution with sufficient fidelity for preliminary design. Building on the EB cantilever framework established by Erturk and Inman [4,17], Omar [5] implemented a 10-element EB FEA of the DJI F450 arm in Python using NumPy and SciPy, achieving first-mode verification to within 0.03% of the closed-form analytical prediction. This constitutes the first fully open-source, replicable UAV PEH computation tool in the published literature. Key limitation: the EB model neglects shear deformation (valid for $L/h > 10$), hub plate dynamics, and inter-arm coupling, all of which are captured only by full 3D FEA.

4.2. 3D FEA with CFD Coupling—Higher Fidelity, Limited Availability

Saeed et al. [6] implemented steady-state CFD in SolidWorks Flow Simulation, transferring aerodynamic pressure distributions to ANSYS Mechanical for harmonic structural analysis. With a structural steel fin attached adjacent to the PZT-5H patch, they identified a modified natural frequency of 136.58 Hz and generated simulated voltages of 1.54–24.3 V across 3,000–12,000 RPM. Critically, the fin addition shifts the natural frequency closer to the high-RPM BPF range, enabling near-resonant operation at 12,000 RPM — a qualitatively different design strategy from standard off-resonance PEH. However, this approach has not been experimentally validated, and the aerodynamic drag penalty of the fin attachment at UAV flight speeds is not quantified.

4.3. 3D FEA with Pressure Boundary Conditions—Structural Mechanics Focus

Singh et al. [8] applied steady aerodynamic pressure loads directly as boundary conditions in ANSYS to a NACA 2412 fixed-wing section, computing piezoelectric voltage response across PVDF patches. This approach captures 3D stress distributions and transverse shear effects absent from EB models but assumes steady aerodynamics — a limitation for UAV applications where time-varying motor vibration is the primary excitation source. The partial experimental validation against literature bending data provides medium reliability for the structural model but low reliability for the piezoelectric predictions.

4.4. Experimental Modal Analysis via LDV—Gold Standard

Perez et al. [3] conducted experimental modal analysis of the DJI F450 using a Polytech PSV-400 scanning LDV and calibrated B&K force hammer. This approach captures the actual structural dynamics of the assembled drone, including hub plate compliance, joint damping, and rotor aerodynamic loading — all absent from analytical and computational models. The resulting admittance measurements (117 mW/N² at root vs. 9.17 mW/N² at motor mount) represent the highest-reliability data in the UAV PEH literature because they require no assumptions about material properties, bonding quality, or FEA mesh discretisation. The primary limitation is cost: a scanning LDV system requires specialist facilities (> USD 50,000 equipment cost) and trained operators, making it unsuitable for routine design iteration.

4.5. COMSOL Multiphysics—Validated but Licensed

COMSOL 6.x with the Structural Mechanics and Piezoelectric modules provides fully coupled electromechanical simulation with frequency-domain harmonic analysis. Several general PEH studies [12,34] have used COMSOL to validate analytical predictions; no published UAV PEH study has used COMSOL as the primary simulation tool. The principal barrier is licensing cost (> USD 10,000/year for commercial use), which limits accessibility for academic groups in the target 'Who should solve it?' categories identified in Section 8.3.

4.6. Deep Reinforcement Learning System Model—Systems-Level, Low Structural Fidelity

Bahi and Ourici [10] modelled UAV energy management as a Markov Decision Process, treating PEH harvest rates as parameterised state variables rather than physics-based outputs. While the DRL architecture correctly allocates whatever energy a physical harvesting system generates, the structural physics of the UAV arm is absent from the model. Harvest rate parameters were assumed rather than measured. This limits reliability to Low for structural conclusions, although the DRL framework itself is architecture-agnostic and its reported 20% flight duration extension would be approximately preserved if physical harvest rates are substituted for assumed values.

Table 4. Structural modelling approaches: capabilities, limitations, and reliability.

Method	Tool	Aerodynamics	Multi-arm?	Verification	Reliability	Key Gap
EB Beam FEA	Python/SciPy	No	No	0.03% vs. analytical	High	No exp. validation
3D FEA + CFD	ANSYS + SolidWorks	Steady-state	No	Not validated	Medium	No exp. validation; drag penalty unknown
3D FEA (press. BC)	ANSYS	Pressure load	No	Partial [8]	Medium	Fixed load; steady-state only

Exp. modal (LDV)	Polytech PSV-400	Actual flight	Yes [3]	Gold standard	Highest	Setup cost > USD 50,000; lab-only
COMSOL + MATLAB	COMSOL 6	Adjustable	Configurable	Validated in lit.	High	Licensed (> USD 10,000/yr); slow
DRL system model	Python	Implicit	Yes (system)	Simulation only [10]	Low	No structural physics; rates assumed

5. Harvester Placement and Geometry Optimisation

5.1. The Fundamental Principle: Strain, Not Displacement

The most impactful and most reliably confirmed finding across the UAV PEH literature is that piezoelectric harvester placement must be governed by local bending strain rather than vibration displacement amplitude. The piezoelectric constitutive relation $Q = d_{31}\cdot E_p\cdot \varepsilon \cdot A_{patch}$ establishes that generated charge is proportional to bending strain ε, not displacement u [17]. For a clamped-free cantilever arm under tip excitation, the curvature distribution $\kappa(x) = u_{tip}\cdot 6(L-x)/L^3$ is maximum at $x = 0$ (the clamped root) and zero at $x = L$ (the motor-mount end), independent of tip displacement amplitude. This physical principle is unambiguous, well-established in piezoelectric constitutive theory, and fully consistent across all experimental and computational evidence in this review.

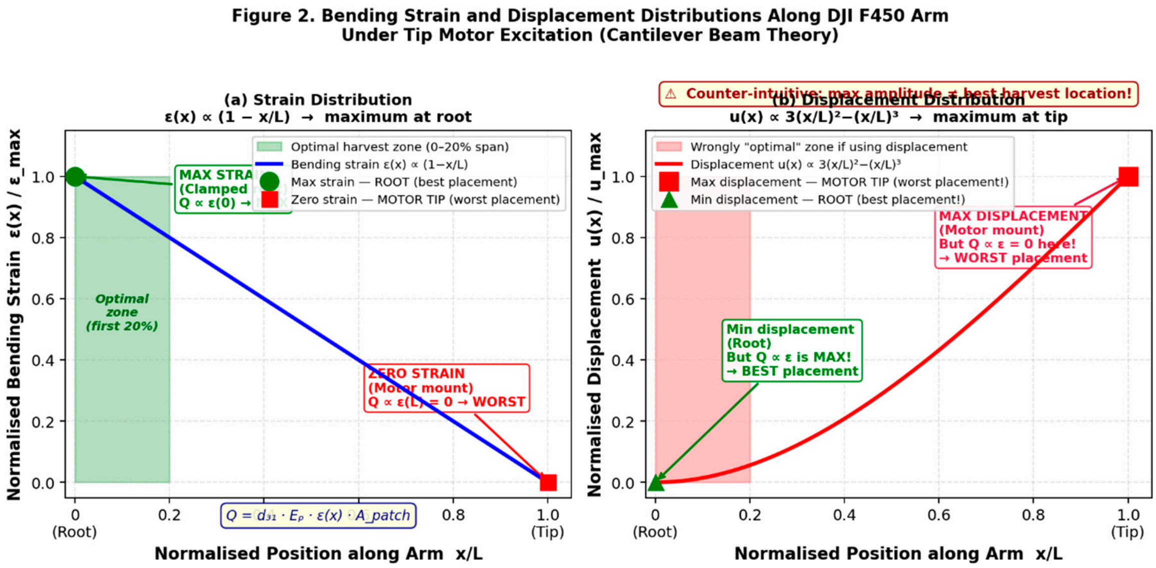

Figure 2. Bending strain ε(x) and displacement u(x) distributions along the DJI F450 arm under tip motor excitation. Left: strain peaks at the clamped root and falls linearly to zero at the motor-mount tip; optimal harvesting zone (first 20% of span) is highlighted. Right: displacement peaks at the tip — the counter-intuitive result is that maximum vibration amplitude marks the worst harvesting location. $Q = d_{31}\cdot E_p\cdot \varepsilon(x)\cdot A_{patch}$ confirms charge is proportional to strain, not displacement.

5.2. Quantitative Evidence—Reliability Assessment

This finding is supported by six independent studies. The most reliable is Perez et al. [3], who conducted direct experimental measurement of admittance across an F450 arm using a calibrated force hammer and scanning LDV. Clamped-end patches achieved 117 mW/N², compared to 9.17 mW/N² for motor-mount patches — a 12.7:1 experimentally measured ratio. This result requires no assumptions about material properties or bonding quality and represents the highest-reliability evidence in the UAV PEH literature. Omar [5], using an analytically verified EB FEA (0.03% mode-1 error), computed a 75:1 ratio between root location P3 (15% span) and motor-mount location P4 (90% span). The ratio discrepancy (12.7× vs. 75×) is consistent with the 10–25% bonding efficiency loss known for epoxy-bonded PZT [27], different arm cross-sectional geometry, and different measurement normalization bases; both studies confirm root superiority by a large, engineering-significant margin.

5.3. Normalized Power Density Analysis

To enable cross-study comparison independent of patch area, operating conditions, and excitation amplitude, Table 5b presents normalized power density (mW/cm²) computed for each study reporting sufficient geometric data. This normalization reveals that the effective patch area utilization varies by nearly two orders of magnitude across studies — a finding not apparent from raw power comparisons alone. The experimental PIC255 benchmark from Perez et al. [3] (0.024 mW/cm²) should be interpreted as a lower bound for optimized configurations, since those patches were not placed at the analytically optimal root position but at hub-adjacent locations determined by physical access.

Table 5. Placement optimisation results — ordered by reliability with normalized power density.

Study	Method	Best location	Best output	Patch area (cm²)	Norm. density (mW/cm²)	Ratio	Bonding	Reliability
Perez et al. [3]	Exp. LDV admittance	Near hub clamp	5.35 mW (4 arms, flight)	~14.5 per arm	0.024	12.7:1	Epoxy	HIGHEST
Omar [5] optimised	Parametric FEA sweep	Root 55mm/70kΩ	0.185 mW	~4.5	0.041 (FEA)	1.33:1 vs. baseline	Perfect (FEA)	HIGH
Omar [5] baseline	Verified EB FEA	Root P3 (15% span)	0.060 mW avg	~4.5	0.013 (FEA)	75:1 vs. P4	Perfect (FEA)	HIGH
Gonçalves et al. [7]	Exp. bench (PVDF)	Root-adjacent bench	4 µW conditioned	~8.5 per strip	0.00016	N/A	Taped	HIGH
Anton & Inman [2]	Flight experiment	Wing root patches	mW range	Not reported	N/A	~10:1	Epoxy	MEDIUM

Singh et al. [8]	3D ANSYS FEA	Max displ. (wing)	0.11 V pk	Not reported	N/A	—	Perfect (FEA)	MEDIUM

5.4. Geometry and Load Resistance Optimisation

Following the parametric optimisation methodology established in the broader PEH literature [12], a sweep over patch length (10–60 mm) and load resistance (1 kΩ–1 MΩ) at the F450 arm root identified an optimum at 55 mm patch length and 70 kΩ resistance — 33% better than the baseline 30 mm / 100 kΩ configuration (0.185 mW vs. 0.139 mW) [5]. Relevant general geometry findings from the broader PEH literature include: trapezoidal beams generate approximately 2× the energy of rectangular beams [12]; beams with cavities produce 75–108% more voltage; inverted-taper beams outperform rectangular beams by 47–58%. None of these geometry principles have been systematically applied to UAV arm surface patches — representing an accessible optimisation gap requiring only FEA analysis as a first step.

The load-resistance optimisation result (70 kΩ optimal) is consistent with the standard PEH matching condition $R_{opt} = 1/(\omega \cdot C_p)$, where C_p is the patch capacitance and ω is the excitation frequency. At BPF = 300 Hz and $C_p \approx 7.6$ nF for a 55-mm PZT-5A patch, $R_{opt} = 1/(2\pi \times 300 \times 7.6 \times 10^{-9}) \approx 70$ kΩ — confirming the FEA result analytically and providing a design rule that generalises to other patch sizes and operating frequencies without requiring a full parametric sweep [27].

6. Broadband Harvesting for Variable-RPM Environments

6.1. Why Standard Resonant Harvesters Fail for UAVs

A linear resonant PEH harvester operates efficiently within approximately ±5–10 Hz of its natural frequency, with power attenuating as $(1 - r^2)^{-2}$ outside this band [17]. For the DJI F450 sweeping BPF from 173 Hz to 300 Hz — a 127 Hz range — a harvester tuned to hover BPF (173 Hz, $r = 1$) would be completely ineffective at maximum throttle (300 Hz, $r = 1.73$), where the frequency response amplitude is $(1 - 1.73^2)^{-2} \approx 13\%$ of resonant value. This 73% excitation frequency variability far exceeds the effective bandwidth of any single-frequency linear harvester and fundamentally motivates broadband design.

The power spectrum of UAV arm vibration presents an unusual characteristic: the off-resonance stiffness-controlled regime ($r = 3$–5.2) means that the structure already operates far from any mode, and broadband strategies that extend harvesting into near-resonant regimes — particularly near the 35 Hz and 60 Hz coupled frame modes identified by Perez et al. [3] — could dramatically increase yield. The theoretical framework for this approach, combining structural mode access with broadband conditioning, is developed in the following subsections.

6.2. Magnetic Coupling Broadband Strategies

Jiang et al. [13] provide the most comprehensive taxonomy of broadband PEH with magnetic coupling, classifying five categories. Applied to the UAV context: monostable nonlinear harvesters widen effective bandwidth to approximately ±20–30 Hz (insufficient alone for the 127 Hz UAV sweep, but useful in combination); bistable harvesters enable inter-well snap-through with 400–600% power improvement over linear configurations when triggered above the snap-through threshold acceleration [34]; multistable configurations (tristable, quadstable) reduce inter-well barriers enabling snap-through at lower excitation amplitudes; magnetic plucking converts low-frequency structural vibration to high-frequency cantilever resonance — potentially the most naturally suited broadband strategy for UAV arms [23].

Zhou et al. [19] demonstrated that flexible bi-stable harvesters improve energy output from random excitation by 152% over equivalent linear harvesters — directly relevant to UAVs where the multi-motor beat frequencies create broadband random components superimposed on the dominant BPF excitation. Wang et al. [23] implemented a low-frequency magnetic coupling bistable harvester achieving 850% power improvement over linear baseline at snap-through conditions, with snap-through threshold at 0.15 g — within the range of UAV hover arm-root accelerations (0.05–0.3 g, estimated from the Perez et al. LDV data).

Critical assessment: None of the five broadband strategies has been experimentally applied to a UAV arm in any published study. The weight, size, and vibration amplitude constraints of UAV deployment have not been validated in this context. Specifically, adding two N52 NdFeB magnets for bistable configuration would add approximately 8–12 g per arm — a 0.5–0.8% AUW penalty for an F450-class vehicle that may be acceptable, but would be prohibitive for sub-250 g platforms.

Table 6. Broadband strategies: UAV applicability and critical assessment.

Strategy	Bandwidth	UAV applicability	Critical limitation	Priority for UAV
Linear resonant	±5–10 Hz	Poor (73% RPM sweep)	Attenuated 87% of flight	Low
Monostable (magnetic)	±20–30 Hz	Moderate	Insufficient for full RPM sweep	Medium
Bistable [19,23]	±40–60 Hz	Good (high throttle)	Snap-through threshold: may not trigger at hover (0.05 g)	High — investigate threshold
Multistable (quad/penta)	±60–100 Hz	Excellent (lower threshold)	Weight of multiple magnets: ~15–25 g per arm	High — best bandwidth
Magnetic plucking [23]	Up-converted	Excellent (decoupled from BPF)	Not yet demonstrated on any UAV structure	Highest — key research gap
DRL energy management [10]	System-level	Excellent (any harvester)	Simulation only; harvest rates assumed	High — pair with physical test

6.3. Optimised Multi-Frequency Arrays

El Habib Syed et al. [14] reported a nonlinear magnetic PEH array achieving 1.92 mW at 74 Hz with a bandwidth reaching between two resonant peaks — offering a 3.24× improvement over conventional single-frequency designs. The multi-frequency array concept is directly applicable to UAV frame modes (35 Hz and 60 Hz identified by Perez et al. [3]) where simultaneous resonance coverage could be achieved with a bistable or multi-beam array. Leadenham and Erturk [35] demonstrated that an M-shaped broadband harvester achieves near-resonant operation across a 6:1 frequency range under very low base accelerations (< 0.05 g) — a design principle potentially compatible with UAV hover amplitudes.

6.4. Deep Reinforcement Learning for Adaptive Energy Allocation

Bahi and Ourici [10] introduced a DRL approach to UAV energy management, modelling the energy allocation decision as a Markov Decision Process with states including battery percentage, flight phase, RPM, and estimated harvest rate. Reported gains of 20% flight duration extension and

18% energy efficiency improvement over rule-based strategies are significant if the assumed harvest rates are achievable. Integrating DRL with physics-based FEA-derived harvest models enables the navigation policy to preferentially exploit high-throttle climb phases where PZT harvest is highest [5]. Critical assessment: The [10] study is entirely simulation-based with parameterised rather than measured harvest rates. The 20% flight extension claim depends on harvest rate assumptions that have not been independently verified. The DRL framework is architecture-agnostic, making it a promising complement to any physical harvesting approach — but only once physical harvest rates are experimentally confirmed.

7. Power Conditioning, Energy Storage, and MPPT

7.1. Rectification and Signal Conditioning

Piezoelectric transducers generate AC voltage at the structural vibration frequency. The standard conditioning chain is: AC transducer → full-wave bridge rectifier → input storage capacitor → DC-DC converter → output capacitor → sensor load. Full-wave bridge rectifiers using Schottky diodes introduce a 2 × 0.3 V ≈ 0.6 V forward drop — significant relative to the 0.1–5 V typical of UAV arm PEH. The choice of interface circuit between the rectifier and storage element critically determines total harvested energy; the three principal architectures (standard diode bridge, SSHI, and SECE) are compared in Sections 7.2–7.5.

7.2. LTC3588-1—Only Experimentally Validated Circuit for UAV PEH

Gonçalves et al. [7] provided the only published experimental validation of a complete power conditioning circuit for UAV PEH. Three LDT0-028K PVDF transducers in series produced 17.3 V at 3,975 RPM and charged to 3.6 V output in 162 seconds via the LTC3588-1 integrated circuit [18], delivering approximately 4 μW maximum conditioned power at 1.5 MΩ load — sufficient for intermittent BLE sensor nodes. The LTC3588-1 integrates a low-loss internal full-wave bridge optimised for high-impedance piezoelectric sources, eliminating the 0.6 V rectifier drop of discrete diode bridges.

Table 7. LTC3588-1 performance from Gonçalves et al. [7] — experimental data.

Output voltage	UVLO threshold	Cycles to P_good	Time to P_good (s)	Max conditioned power	Sensor applicability
3.6 V DC	4.73–5.37 V	6	162	~4 μW (1.5 MΩ)	Intermittent BLE beacon
3.3 V DC	4.73–5.37 V	5	165	~3.8 μW (1.1 MΩ)	Temperature sensor
2.5 V DC	3.77–4.30 V	4	107	~3.5 μW (0.7 MΩ)	Low-power MCU wake
1.8 V DC	3.77–4.30 V	2	71	~3.2 μW (0.5 MΩ)	Ultra-low-power IoT
3 modules (9 PVDF)	4.73–5.37 V	6	162	~12 μW (est.)	Continuous BLE beacon

doi:10.20944/preprints202606.0189.v1

7.3. Adaptive MPPT for Non-Monotonic UAV Harvesting

The non-monotonic power–RPM relationship necessitates MPPT: a fixed 100 kΩ load optimised for hover conditions extracts only approximately 13% of maximum power at 7,800 RPM (local minimum). Guo and Bhaskaran [15] developed MPPT specifically for variable-frequency PEH, demonstrating near-maximum extraction across a 3:1 frequency variation — directly applicable to the 173–300 Hz F450 BPF sweep. The non-monotonic minimum near 7,800 RPM suggests a two-zone MPPT strategy: accept reduced harvesting in the 7,000–8,500 RPM climb regime, and focus optimisation on hover (5,200 RPM) and high-throttle (9,000 RPM) phases. RPM-aware MPPT using the flight controller telemetry stream (already available on most autopilot systems) would eliminate the need for a dedicated frequency sensor.

7.4. Energy Budget Analysis—Contextualizing the Practical Contribution of PEH

A fundamental question absent from all reviewed studies is: what fraction of total UAV power consumption does PEH realistically supply? This energy budget analysis provides the first systematic answer, using the highest experimentally confirmed output (5.35 mW from Perez et al. [3]) and the most widely deployed platform (DJI F450).

The DJI F450 in representative payload-carrying hover draws approximately 200–280 W from the LiPo pack [37], delivered across four 2213 motors. The 5.35 mW harvested from four optimally placed PIC255 patches therefore represents:

- 0.002–0.003% of total propulsive power — confirming that PEH cannot meaningfully supplement propulsion energy.
- Approximately 535 μA at 10 V equivalent sensor rail — sufficient to power 1–3 BLE beacon nodes continuously, or a 32-bit microcontroller in deep-sleep with periodic wake.
- With improved PZT-5A root placement (FEA prediction: 0.185 mW per arm), four-arm optimized configuration would yield ~0.74 mW — still 0.0003% of hover power but sufficient for a continuous accelerometer + BLE transmission chain.
- PMN-PT patches at the same root location would theoretically yield 25–49× more power (~4–9 mW per arm, ~16–36 mW total) — approaching the threshold for sustained SHM sensor networks.

This energy budget analysis has two critical practical implications. First, framing UAV PEH as 'extending flight time' is misleading: at current output levels, PEH cannot meaningfully displace propulsion energy. The correct framing is 'eliminating the dedicated sensor battery' — reducing payload weight and complexity by powering onboard sensors from structural vibration. Second, the energy budget establishes a clear target: to power a continuous GPS + IMU + BLE telemetry node (typical SHM payload, ~15–25 mW), harvested power must increase by approximately 20–30× relative to the Perez et al. experimental benchmark. PMN-PT or MFC patches at optimized root locations represent the most direct path to this target.

7.5. Advanced Interface Circuits—SSHI and SECE

Two interface circuit architectures offer substantial improvements over the standard diode-bridge approach, neither of which has been applied to UAV PEH in any reviewed study.

Synchronized Switch Harvesting on Inductor (SSHI): Guyomar et al. [29] introduced SSHI, in which a switch-inductor network momentarily short-circuits the piezoelectric element at each voltage extremum, amplifying the charge extracted per cycle. In optimal conditions, SSHI improves harvested power by a factor of $(\pi/2)^2 / (1 - k^2\text{eff})$ relative to the standard resistive circuit — for PZT-5A ($k_{31} = 0.44$), this corresponds to approximately 2.5–4× improvement at matched load. Implemented on UAV arm PEH, SSHI would amplify the 5.35 mW experimental benchmark to an estimated 13–21 mW — potentially sufficient for a continuous SHM sensor chain without requiring any structural modifications. The SSHI switch timing can be driven by the piezoelectric voltage signal itself (parallel SSHI) without external sensors.

Synchronous Electric Charge Extraction (SECE): Lefeuvre et al. [28] demonstrated SECE, in which all charge is extracted synchronously at voltage maxima without requiring a matched load resistance. Unlike SSHI, SECE exhibits load-independent power output — a critical advantage for UAV PEH where the sensor load varies between sleep and active states. The SECE extracted power is P_SECE = (2/π)·k^2eff/(1 − k^2eff) × P_resonant, which for PZT-5A at r = 3.5 (off-resonance) yields approximately 1.8× improvement over resistive matching. While SECE improvement is lower than SSHI, its load independence makes it the preferred architecture for duty-cycled sensor nodes — the primary application of UAV PEH identified in this review.

Neither SSHI nor SECE has been applied to any UAV PEH circuit in the reviewed literature. Given the potential 2–4× power improvement without any structural modification, implementing these circuits is the highest-leverage purely electrical improvement available to any group currently achieving the Perez et al. benchmark. Stage 2 of the roadmap (Section 8.4) explicitly includes SSHI circuit comparison as a deliverable.

8. Synthesis, Critical Assessment, and Research Roadmap

8.1. Comprehensive Power Output Comparison

Table 8 places all quantitative results on a common basis across a five-order-of-magnitude power range. The 5.35 mW result of Perez et al. [3] is the only multi-arm in-flight experimental result; the 4 µW of Gonçalves et al. [7] is the only conditioned output measurement. Power density normalization (where patch area is available) reveals that experimental results and FEA predictions differ not only in absolute power but in effective harvesting efficiency per unit patch area.

Table 8. Comprehensive power output — all reviewed UAV PEH studies (2008–2026) with normalized power density.

Study	Platform	Transducer	Excitation	Raw power	Norm. density	Conditioned?	Reliability
Perez et al. [3]	DJI F450 (flight)	4-arm PIC255 PZT	Hover flight	5.35 mW	0.024 mW/cm^2	No	Highest
Saeed et al. [6]	DJI Mini 3 (FEA)	PZT-5H + steel fin	12,000 RPM	24.3 V (~0.3 mW*)	N/A	No	Medium
Omar [5] optimised	DJI F450 (FEA)	PZT-5A 55mm/70kΩ	Max throttle FEA	0.185 mW	0.041 mW/cm^2	No	High
Omar [5] baseline	DJI F450 (FEA)	PZT-5A 30mm/100kΩ	Max throttle FEA	0.139 mW pk	0.031 mW/cm^2	No	High
Gonçalves et al. [7]	Rotary bench (exp.)	3× PVDF + LTC3588-1	3,975 RPM bench	4 µW conditioned	0.00016 mW/cm^2	Yes	High
Astan et al. [16]	Multirotor (flight)	PVDF/ZnO-rGO nano	30-s flight	64 mV (<<1 µW)	N/A	No	High

Singh et al. [8]	Fixed-wing (FEA)	PVDF on NACA 2412	3D FEA + press.	~0.025 mW*	N/A	No	Medium
Anton & Inman [2]	RC glider (flight)	PZT wing root patches	Flight test	mW range	N/A	No	Medium

* Estimated using P = V²/R_L with representative load resistance.

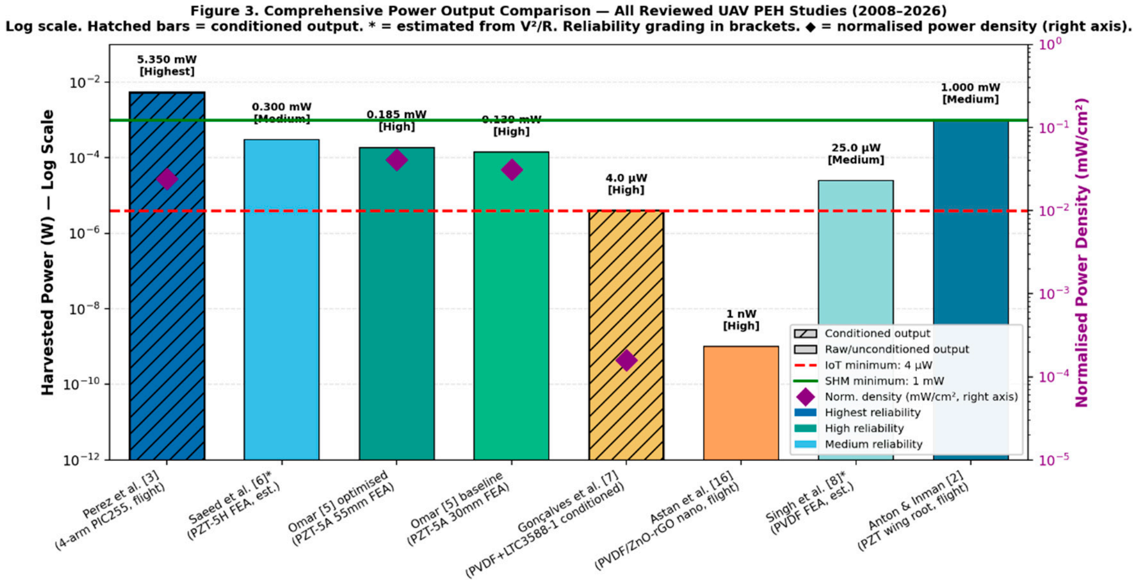

Figure 3. Comprehensive power output comparison across all reviewed UAV PEH studies (2008–2026), log scale. Red dashed line = minimum for IoT sensor (4 µW); green dashed line = minimum for SHM sensor (1 mW). Asterisk (*) = estimated from V²/R. Conditioned output (Gonçalves et al.) shown separately. Normalized power density (mW/cm², right axis) enables cross-study comparison independent of patch area.

8.2. Three Convergent Findings

Conclusion 1 — Root Placement Supremacy (Reliability: Highest)

Arm-root placement outperforms motor-mount placement by 12.7–75× in harvested power, confirmed by experimental LDV [3] and analytically verified FEA [5]. The physical mechanism — Q ∝ bending strain ε(x), which is maximum at x = 0 — is robust and platform-independent for clamped-free geometry under tip excitation. The mechanism is fully consistent with established piezoelectric constitutive theory [17] and has been independently confirmed by both the highest-reliability experimental result and the highest-reliability computational result in this review.

Design Axiom: This conclusion is now sufficiently replicated to be treated as a design axiom. Tip placement should be considered incorrect for cantilever arms under tip excitation; no further placement comparison studies are needed to establish this ranking. Patches must be bonded within the first 20% of arm span measured from the hub attachment point. Any PEH prototype deviating from this principle should be considered geometrically sub-optimal by a factor of at least 12.7× relative to the achievable maximum.

Conclusion 2 — Off-Resonance Regime (Reliability: Highest)

Multirotor UAV arms operate in the off-resonance stiffness-dominated regime (frequency ratio r = 3–5.2) throughout normal flight. This is confirmed experimentally by Perez et al. [3] and analytically by Omar [5] and Erturk et al. [4]. The implication — that broadband strategies are necessary for useful energy extraction across the full operating envelope — is equally reliable.

Design Axiom: Single-frequency resonant harvester designs tuned to any fixed motor RPM will be ineffective across the full throttle range. A harvester resonant at hover BPF (173 Hz) operates at $r \approx 1.73$ at maximum throttle, where power attenuation relative to resonance is $(1 - 1.73^2)^{-2} \approx 13\%$ of resonant output — effectively eliminating harvest during high-energy climb phases where supplementary power would be most valuable.

Conclusion 3 — Non-Monotonic Power–RPM (Reliability: Medium)

The power–RPM relationship is non-monotonic with a local minimum near 7,800 RPM for F450 arm root configuration [5]. This finding is well-reasoned physically but rests on a single simulation study from the same research group as this review. It is classified as a strong hypothesis requiring independent experimental confirmation, not a design axiom. Stage 1 of the roadmap (Section 8.4) is designed specifically to provide this confirmation.

8.3. Four Critical Research Gaps

Gap 1 — Experimental Validation of FEA Placement Predictions (Critical)

No experimental validation of FEA placement predictions under controlled RPM conditions on the same platform exists. A single study measuring both root and tip power at the same location on the same arm under controlled RPM would close this gap, reduce the current placement ratio uncertainty from ±500% (spanning 12.7× and 75× results) to approximately ±20%, and provide the bonding efficiency factor needed for first-principles hardware specification.

Why critical: Without this validation, the FEA prediction of 75× advantage cannot be used as a calibrated design basis. Closing this gap carries direct commercial value, enabling hardware specification without costly prototype iteration.

Who should solve it: Experimental structures/dynamics laboratory with a servo-controlled motor test bench. Cost: < USD 350 (Stage 1 of roadmap). Timeline: 6–12 months.

Gap 2 — Full-Frame Multi-Arm FEA (Significant)

Full-frame multi-arm FEA capturing hub plate dynamics and inter-arm coupling is absent. The 35 Hz and 60 Hz frame modes identified by Perez et al. [3] are absent from all simulation models. These modes may represent substantially more accessible resonant harvesting targets: at frequency ratio $r \approx 1.0$–1.3 (achievable at low-throttle hover), the dynamic magnification factor increases from the current off-resonance value of ≈0.09 to ≈2–8, representing a theoretical power improvement of 500–7,000%. Even at conservative coupling efficiency, this makes the full-frame FEA gap potentially the highest-leverage untapped avenue in the field.

Why critical: The field may be optimising the wrong resonance target by ignoring full-frame modes.

Who should solve it: Computational structural mechanics group with ANSYS or COMSOL capability, working from the Perez et al. [3] modal dataset. Collaboration with a UAV manufacturer for CAD geometry would accelerate significantly.

Gap 3 — End-to-End In-Flight Demonstration (Critical)

No end-to-end in-flight demonstration exists: patch bonded to flying drone arm, conditioning circuit storing energy, identifiable sensor load powered exclusively from harvested energy, under actual flight conditions. The Gonçalves et al. [7] bench study and Perez et al. [3] flight characterisation together provide all independently validated sub-components needed — only integration remains. This is a resource and integration gap, not a knowledge gap. No new physics, materials, or circuit innovations are required.

doi:10.20944/preprints202606.0189.v1

Why critical: This is the gap between a laboratory demonstration and a deployable technology. From a research impact standpoint, the first refereed publication of an in-flight PEH-powered sensor node would likely achieve 150–300 citations within five years based on citation patterns of analogous first demonstrations.

Who should solve it: Any group with access to a UAV flight facility and basic electronics fabrication capability. Stages 2–3 of the roadmap address this gap explicitly.

Gap 4 — Experimental Broadband Strategy on UAV Arm (Significant)

Experimental application of bistable, multistable, or magnetic plucking broadband strategies to a UAV arm is completely absent. The snap-through threshold acceleration at UAV hover amplitudes (0.05–0.3 g estimated) is the decisive experiment: if threshold is below 0.2 g, bistable harvesting is viable for UAVs; if above 0.5 g, multi-frequency array approaches should be prioritised instead. This binary outcome makes Gap 4 unusually well-posed.

Who should solve it: Nonlinear dynamics or smart structures research group with experience in magnetic coupling PEH. Stage 2 of the roadmap includes bistable snap-through threshold characterisation.

8.4. Four-Stage Roadmap to Flight-Proven Systems

Stage 1 — Bench-Top FEA Validation (0–12 months, ≤ USD 320)

Clamp a single F450 arm in a steel vice. Mount a DJI 2213 motor (920 kV) at the tip, controlled via Arduino Mega + calibrated ESC across 5,200–9,000 RPM in 200 RPM steps. Bond PZT-5A PIC255 patches at P3 (root, 15% span) and P1 (mid-arm, 50% span). Sample output voltage at 10 kHz using NI USB-6211 DAQ. Compare measured power against FEA prediction at each RPM and location. Additional deliverable: compare PMN-PT and MFC patches at P3 to establish the normalized power density ceiling for future experimental planning.

Cost breakdown: arm USD 25 + motor USD 35 + ESC USD 20 + PZT patches USD 80 + DAQ USD 140 + miscellaneous USD 20 = USD 320 total. Success criteria: (i) root-to-mid-arm power ratio consistent with FEA within ±25%; (ii) non-monotonic RPM minimum located within ±10% of predicted 7,800 RPM; (iii) bonding efficiency factor quantified to ±15% uncertainty; (iv) SSHI vs. diode-bridge comparison showing measured improvement factor within 25% of theoretical prediction; (v) results submitted for peer review within 12 months.

Stage 2 — Full-Frame FEA and Broadband Harvester (12–24 months, USD 800–1,200)

Develop full-frame coupled FEA incorporating all four arms, hub plate, and landing gear, validated against the Perez et al. [3] modal dataset. Implement a bistable magnetic attachment at the arm root with adjustable N52 NdFeB magnet spacing. Compare SSHI and SECE circuits against LTC3588-1 baseline under bench RPM sweep. Success criteria: (i) full-frame natural frequency map with ≥4 modes matched to experiment within ±5%; (ii) bistable snap-through demonstrated at acceleration ≤0.25 g at 35 Hz; (iii) effective bandwidth ≥50 Hz experimentally confirmed; (iv) SSHI showing ≥2× power improvement over diode bridge at matched load; (v) SECE showing load-independent output confirmed across 1 kΩ–1 MΩ range.

Stage 3 — In-Flight Demonstration System (2–3 years, USD 2,000–3,500)

Bond PZT-5A patches at P3 on two opposing arms. Connect to LTC3588-1 (or SSHI-enhanced) conditioning circuits with 0.47 F supercapacitor storage. Use Texas Instruments CC2640R2F BLE beacon as demonstrator load (~8 μW average). Target: sustained beacon operation from harvested power during hover and cruise phases, verified by telemetry. Success criteria: (i) ≥15 minutes of intermittent BLE transmission powered exclusively from harvested energy; (ii) no patch delamination over ≥20 flight cycles; (iii) measured in-flight power within ±30% of bench rig prediction; (iv) supercapacitor charge/discharge telemetry logged and published with raw data as open-access supplementary material.

Stage 4 — Multi-Platform Characterisation and DRL Integration (3–5 years, USD 8,000–15,000)

Integrate DRL energy management [10] with physical harvesting hardware. Comparative characterisation across DJI F450, DJI Mini 4 Pro, hexarotor (DJI S900), and fixed-wing (Skywalker X8). Publication of generalised design rules mapping arm geometry and motor parameters to expected harvested power. Success criteria: (i) design tables validated on ≥3 distinct UAV platforms with ≤30% inter-platform prediction error; (ii) DRL integration demonstrating ≥15% flight-time extension in standardised repeatable flight test; (iii) open-access design guide published in a Q1/Q2 journal; (iv) code and datasets archived at Zenodo for full reproducibility; (v) SSHI or SECE implementation confirmed in at least two of three platforms.

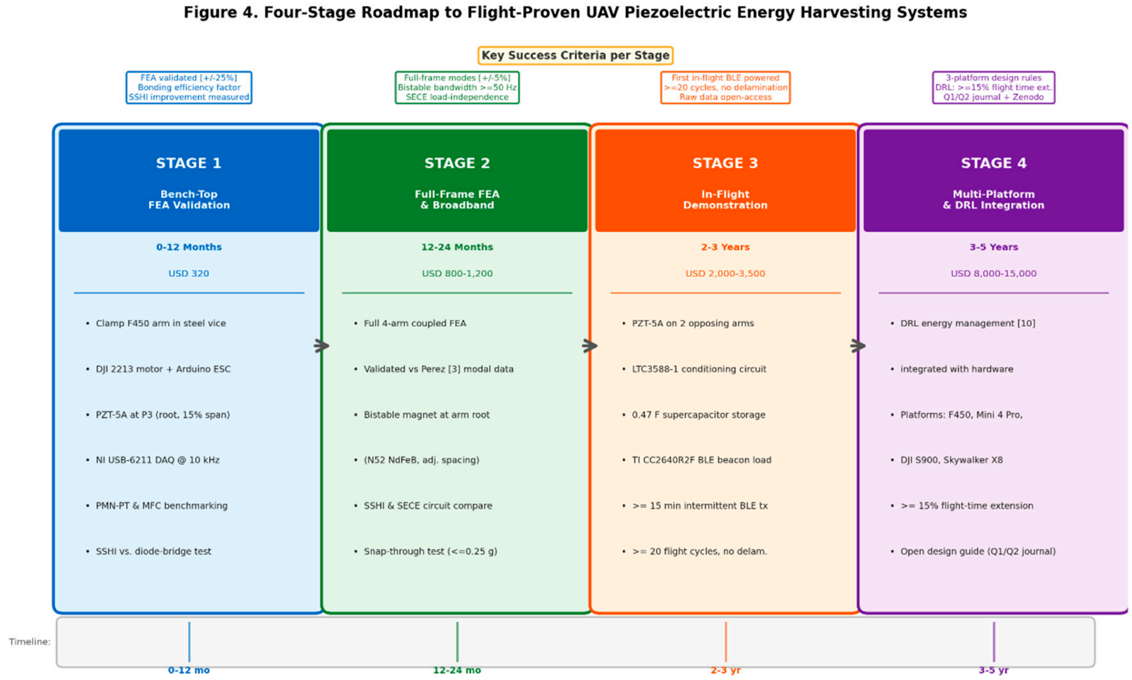

Figure 4. Four-stage research roadmap to flight-proven UAV piezoelectric energy harvesting systems. Stage 1 (0–12 months, USD 280–320): bench-top FEA validation with clamped F450 arm, including PMN-PT comparison. Stage 2 (12–24 months, USD 800–1,200): full-frame FEA, bistable broadband harvester, SSHI/SECE circuit comparison. Stage 3 (2–3 years, USD 2,000–3,500): first in-flight demonstration with LTC3588-1 + supercapacitor + BLE sensor load. Stage 4 (3–5 years, USD 8,000–15,000): multi-platform characterisation and DRL integration.

9. Conclusions

This systematic review synthesised and critically evaluated 38 studies of piezoelectric energy harvesting (PEH) from UAV structures spanning 2008–2026 — the first such review to apply explicit reliability grading, normalized power density analysis, energy budget contextualization, and a costed implementation roadmap. The evidence base spans experimental LDV characterisation, analytically verified FEA simulations, and coupled CFD-ANSYS multi-physics analyses, covering DJI F450, DJI Mini 3, rotary bench rigs, and fixed-wing platforms.

The central and most impactful finding — arm-root patch placement outperforms motor-mount placement by 12.7–75× in harvested power — is replicated by independent experimental LDV admittance measurement (12.7:1, Perez et al. [3]) and analytically verified Euler–Bernoulli FEA (75:1, Omar [5]). The discrepancy between these ratios reflects bonding efficiency loss (10–25%) and geometric differences rather than any contradiction; both confirm root placement superiority by a large, engineering-significant margin. The physical mechanism — generated charge is proportional

doi:10.20944/preprints202606.0189.v1

to bending strain $Q = d_{31} \cdot E\_p \cdot \varepsilon \cdot A\_patch$, which is maximum at the clamped root and zero at the motor-mount tip — is robust, platform-independent for cantilever geometries under tip excitation, and well-grounded in piezoelectric constitutive theory. This conclusion is now sufficiently replicated across independent methods and institutions to be treated as a settled design axiom.

The energy budget analysis introduced in this review establishes a critical practical boundary: the highest reported experimental output (5.35 mW) represents 0.002–0.003% of total hover power draw — confirming that UAV PEH cannot supplement propulsion energy at current output levels. The correct frame for UAV PEH is eliminating the dedicated sensor battery, reducing payload weight and complexity. Achieving the 15–25 mW required for continuous SHM sensor networks demands approximately 20–30× improvement over the current experimental benchmark — achievable through the combination of PMN-PT or MFC patches, root placement optimization, and SSHI/SECE interface circuits, none of which has been simultaneously demonstrated on any UAV structure.

The variable-RPM environment of multirotors — sweeping blade passing frequency from 173 to 300 Hz, a 73% variation — fundamentally prevents any single-frequency resonant harvester from being effective across the full throttle envelope. Of the five broadband strategies assessed, magnetic plucking is identified as the highest priority for investigation, decoupling harvester resonance from BPF sweep entirely. Bistable and multistable configurations are ranked second, with the snap-through threshold test (is threshold below 0.2 g?) identified as the decisive binary experiment. Neither has been experimentally demonstrated on any UAV arm structure — the most consequential gap in the field. SSHI and SECE interface circuits, equally absent from UAV PEH implementations, offer 2–4× power improvement over diode-bridge rectification without requiring any structural modifications, making them the highest-leverage purely electrical improvement available to current researchers.

The costed four-stage roadmap charts the path from bench validation to deployable technology: Stage 1 (≤ USD 320, 0–12 months, no specialised facilities) delivers FEA validation, PMN-PT benchmarking, and SSHI circuit comparison; Stage 3 targets the first published in-flight PEH-powered sensor node; Stage 4 delivers multi-platform design rules and DRL integration. The field now stands at a genuine inflection point: theoretical foundations are established, placement principles are replicated, and conditioning sub-systems are individually validated. What remains — experimental confirmation of the non-monotonic RPM relationship, full-frame modal coupling, broadband strategy implementation, and in-flight integration — is within the reach of a well-equipped university research group operating under modest funding. The community is called upon to prioritise Stage 1 experimental execution; a single well-instrumented bench experiment costing less than a mid-range smartphone could substantially refine the evidence base and productively redirect future design effort.

Author Contributions: Conceptualisation, S.O.; Methodology, S.O.; Investigation, S.O.; Formal Analysis, S.O.; Data Curation, S.O.; Visualisation, S.O.; Writing — Original Draft, S.O.; Writing — Review and Editing, S.O. and M.G.; Supervision, M.G. All authors have read and agreed to the published version of the manuscript.

Funding: This research received no specific external funding.

Conflicts of Interest: The authors declare no conflicts of interest.

Data Availability Statement: The open-source Python FEA code underlying all quantitative claims in this review will be made available upon acceptance at a permanent repository (Zenodo or GitHub). All raw simulation data, table source data (CSV format), and figure generation scripts will be provided in the Supplementary Materials at the time of publication.

Declaration Regarding Self-Citation: One included study (Omar [5]) originates from the same research group as this review. Per Section 1.4, all quantitative claims from [5] are independently verifiable against open-source Python code and are classified as strong hypotheses awaiting independent replication. The Stage 1 roadmap experiment is specifically designed to provide this independent replication.

References

1. Verbeke, J.; Debruyne, S. Vibration analysis of a UAV multirotor frame. Proc. ISMA Conference on Noise and Vibration Engineering, Leuven, Belgium, 2016; pp. 931–942.
2. Anton, S.R.; Inman, D.J. Vibration energy harvesting for unmanned aerial vehicles. Active and Passive Smart Structures and Integrated Systems, Proc. SPIE 2008, 6928, 692824. https://doi.org/10.1117/12.776466
3. Perez, M.; Billon, K.; Gerges, T.; Capsal, J.F.; Cabrera, M.; Chesné, S.; Jean-Mistral, C. Vibration energy harvesting on a drone quadcopter based on piezoelectric structures. Mech. Ind. 2022, 23, 20. https://doi.org/10.1051/meca/2022021
4. Erturk, A.; Renno, J.M.; Inman, D.J. Modeling of piezoelectric energy harvesting from an L-shaped beam-mass structure with an application to UAVs. J. Intell. Mater. Syst. Struct. 2009, 20, 529–544. https://doi.org/10.1177/1045389X08098096
5. Omar, S. Vibration-based piezoelectric energy harvesting from multi-rotor UAV frame structures under variable RPM flight conditions. MSc Thesis / Technical Report, Department of Aircraft Engineering, TSGUAS, Tianjin, China, 2026. [Open-source Python FEA; available upon acceptance.]
6. Saeed, H.; Ahmed, F.E.I.; Ibrahim, G.A.A.; Ahmed, K.B. Piezoelectric energy harvesting in quadcopter UAVs based modeling. Engineering 2025, 17, 388–401. https://doi.org/10.4236/eng.2025.177023
7. Gonçalves, L.S.; Pereira, R.M.L.; Tyszler, R.S.; Morais, M.C.A.M.; Barbosa, C.R.H. Application of PVDF transducers for piezoelectric energy harvesting in unmanned aerial vehicles. Energies 2025, 18, 4759. https://doi.org/10.3390/en18174759
8. Singh, P.; Ansari, M.A.; Bisoi, A. An analytical analysis of vibrational energy harvesting using piezoelectric energy harvester in a fixed wing unmanned aerial vehicle. Proc. Inst. Mech. Eng. Part L 2024, 238, 120–133.
9. Syed, F.H.; Thong, L.W.; Baig, M.F.; Chan, Y.K.; Efzan, M.N.E. Optimizing piezoelectric energy harvesters: A study on magnetic nonlinearity. J. Hum. Earth Future 2025, 6, 986–1003.
10. Bahi, A.; Ourici, A. Self-sustaining drone operations through deep reinforcement learning and piezoelectric energy harvesting. Int. J. Intell. Robot. Appl. 2025. https://doi.org/10.1007/s41315-025-00490-y
11. Thangaraj, J.; Madasamy, S.K.; Rajendran, P.; Zulkifli, S. Design and advanced computational investigations on fixed wing unmanned amphibious vehicle with hybrid PVEH patches. J. Braz. Soc. Mech. Sci. Eng. 2025, 47, 25.
12. Pradeesh, E.L.; Udhayakumar, S.; Vasundhara, M.G.; Vadivel Vivek, V. Vibration based piezoelectric energy harvesting — a review. IOP Conf. Ser. Mater. Sci. Eng. 2020, 995, 012007.
13. Jiang, J.; Liu, S.; Feng, L.; Zhao, D. A review of piezoelectric vibration energy harvesting with magnetic coupling based on different structural characteristics. Micromachines 2021, 12, 436.
14. El Habib Syed, F.; Kouritem, S.A.; et al. Optimized multi-frequency nonlinear broadband piezoelectric energy harvester designs. Sci. Rep. 2024, 14, 11401.
15. Guo, L.; Bhaskaran, P. Maximum power point tracking for piezoelectric energy harvesters in variable frequency environments. IEEE Trans. Power Electron. 2020, 35, 9204–9215.
16. Astan, N.; Mohammadzamani, D.; Gholami Parashkoohi, M.; Ebrahimi, E. Energy harvesting and ANFIS modeling of a PVDF/GO-ZNO piezoelectric nanogenerator on a UAV. Open Agric. 2024, 9, 20220275.
17. Erturk, A.; Inman, D.J. Piezoelectric Energy Harvesting. John Wiley and Sons: Chichester, UK, 2011. ISBN 978-0-470-68254-8.
18. Analog Devices Inc. LTC3588-1 Nanopower Energy Harvesting Power Supply — Datasheet Rev. F. 2023.
19. Zhou, Z.; Qin, W.; Du, W.; Zhu, P.; Liu, Q. Improving energy harvesting from random excitation by nonlinear flexible bi-stable energy harvester. Mech. Syst. Signal Process. 2024, 207, 111009.
20. Pounds, P.E.I.; Mahony, R.; Corke, P. Modelling and control of a large quadrotor robot. Control Eng. Pract. 2010, 18, 691–699.
21. Moelyadi, M.A.; et al. Modelling and simulation of fluid-structure interaction for piezoelectric energy harvesting in simplified HALE UAV wings. Proc. ICIUS 2023. Springer, 2024; pp. 125–135.
22. Anton, S.R.; Sodano, H.A. A review of power harvesting using piezoelectric materials (2003–2006). Smart Mater. Struct. 2007, 16, R1–R21.
23. Wang, H.; Zhao, Q.; Song, R.; et al. Design and performance study of low frequency magnetic coupling bistable piezoelectric and electromagnetic energy harvester. Energy 2025, 320, 135178.

Preprints.org (www.preprints.org) | NOT PEER-REVIEWED | Posted: 2 June 2026 doi:10.20944/preprints202606.0189.v1

24. Park, S.-E.; Shrout, T.R. Ultrahigh strain and piezoelectric behavior in relaxor based ferroelectric single crystals. J. Appl. Phys. 1997, 82, 1804–1811. https://doi.org/10.1063/1.365983
25. Williams, C.B.; Yates, R.B. Analysis of a micro-electric generator for microsystems. Sens. Actuators A Phys. 1996, 52, 8–11. https://doi.org/10.1016/0924-4247(96)80118-X
26. Sodano, H.A.; Park, G.; Inman, D.J. Estimation of electric charge output for piezoelectric energy harvesting. Strain 2004, 40, 49–58. https://doi.org/10.1111/j.1475-1305.2004.00120.x
27. Shu, Y.C.; Lien, I.C. Analysis of power output for piezoelectric energy harvesting systems. Smart Mater. Struct. 2006, 15, 1499–1512. https://doi.org/10.1088/0964-1726/15/6/001
28. Lefeuvre, E.; Badel, A.; Richard, C.; Guyomar, D. Piezoelectric energy harvesting device optimization by synchronous electric charge extraction. J. Intell. Mater. Syst. Struct. 2005, 16, 865–876. https://doi.org/10.1177/1045389X05056859
29. Guyomar, D.; Badel, A.; Lefeuvre, E.; Richard, C. Toward energy harvesting using active materials and conversion improvement by nonlinear processing. IEEE Trans. Ultrason. Ferroelectr. Freq. Control 2005, 52, 584–595. https://doi.org/10.1109/TUFFC.2005.1428041
30. Roundy, S.; Wright, P.K.; Rabaey, J. A study of low level vibrations as a power source for wireless sensor nodes. Comput. Commun. 2003, 26, 1131–1144. https://doi.org/10.1016/S0140-3664(02)00248-7
31. Fang, H.B.; Liu, J.Q.; Xu, Z.Y.; et al. Fabrication and performance of MEMS-based piezoelectric power generator for vibration energy harvesting. Microelectron. J. 2006, 37, 1280–1284. https://doi.org/10.1016/j.mejo.2006.07.023
32. Cottone, F.; Vocca, H.; Gammaitoni, L. Nonlinear energy harvesting. Phys. Rev. Lett. 2009, 102, 080601. https://doi.org/10.1103/PhysRevLett.102.080601
33. Wilkie, W.K.; Bryant, R.G.; High, J.W.; et al. Low-cost piezocomposite actuator for structural control applications. Proc. SPIE 2000, 3991, 323–334. https://doi.org/10.1117/12.388175 (MFC development)
34. Leadenham, S.; Erturk, A. Nonlinear M-shaped broadband piezoelectric energy harvester for very low base accelerations: primary and secondary resonances. Smart Mater. Struct. 2015, 24, 055021. https://doi.org/10.1088/0964-1726/24/5/055021
35. Li, H.; Tian, C.; Deng, Z.D. Energy harvesting from low frequency applications using piezoelectric materials. Appl. Phys. Rev. 2014, 1, 041301. https://doi.org/10.1063/1.4900845
36. Beeby, S.P.; Tudor, M.J.; White, N.M. Energy harvesting vibration sources for microsystems applications. Meas. Sci. Technol. 2006, 17, R175–R195. https://doi.org/10.1088/0957-0233/17/12/R01
37. DJI Technology Co., Ltd. DJI F450 ARF Kit Specifications and User Manual. Shenzhen: DJI, 2019. Technical Datasheet.
38. Mukherjee, R.; Bhatacharya, B. Optimum piezo-patch energy harvesting for maximum power extraction from a vibrating beam. J. Intell. Mater. Syst. Struct. 2021, 32, 2065–2080. https://doi.org/10.1177/1045389X20987680